Article

Strange-metal behaviour in a pure ferromagnetic Kondo lattice

https://doi.org/10.1038/s41586-020-2052-z

Received: 30 July 2019

Accepted: 11 December 2019

Published online: 4 March 2020

Check for updates

Bin Shen[1,7], Yongjun Zhang[1,7], Yashar Komijani[2], Michael Nicklas[3], Robert Borth[3], An Wang[1], Ye Chen[1], Zhiyong Nie[1], Rui Li[1], Xin Lu[1], Hanoh Lee[1,6], Michael Smidman[1]✉, Frank Steglich[1,3], Piers Coleman[2,4]✉ & Huiqiu Yuan[1,5]✉

A wide range of metals exhibit anomalous electrical and thermodynamic properties when tuned to a quantum critical point (QCP), although the origins of such strange metals have posed a long-standing mystery. The frequent association of strange metals with unconventional superconductivity and antiferromagnetic QCPs[1–4] has led to the belief that they are highly entangled quantum states[5]. By contrast, ferromagnets are regarded as an unlikely setting for strange metals, because they are weakly entangled and their QCPs are often interrupted by competing phases or first-order phase transitions[6–8]. Here we provide evidence that the pure ferromagnetic Kondo lattice[9,10] $CeRh_6Ge_4$ becomes a strange metal at a pressure-induced QCP. Measurements of the specific heat and resistivity under pressure demonstrate that the ferromagnetic transition is continuously suppressed to zero temperature, revealing a strange-metal behaviour around the QCP. We argue that strong magnetic anisotropy has a key role in this process, injecting entanglement in the form of triplet resonating valence bonds into the ordered ferromagnet. We show that a singular transformation in the patterns of the entanglement between local moments and conduction electrons, from triplet resonating valence bonds to Kondo-entangled singlet pairs at the QCP, causes a jump in the Fermi surface volume—a key driver of strange-metallic behaviour. Our results open up a direction for research into ferromagnetic quantum criticality and establish an alternative setting for the strange-metal phenomenon. Most importantly, strange-metal behaviour at a ferromagnetic QCP suggests that quantum entanglement—not the destruction of antiferromagnetism—is the common driver of the varied behaviours of strange metals.

Quantum materials that are augmented by strong electronic correlations are promising for various applications, but the electronic interactions that empower these materials challenge our understanding. One of the most pressing questions in strongly correlated electronic systems is the origin of the strange-metal behaviour that develops at a quantum critical phase transition between a delocalized Fermi liquid, and a localized or partially localized electronic phase. A prime example is the strange-metal behaviour that develops in the normal state of copper oxide superconductors at optimal doping, characterized by a robust linear resistivity and a logarithmic temperature dependence of the specific-heat coefficient[2,3]; similar behaviour is also observed in various quantum critical heavy electron materials. The underlying universality of strange-metal behaviour that develops in the vicinity of QCPs is currently a subject of intense theoretical interest. One of the valuable ways of identifying the key ingredients of strange-metal behaviour is through experiments that explore new classes of quantum materials.

Kondo lattice systems, which have periodically arranged atoms hosting localized *f* electrons show a rich variety of properties, owing to competition between magnetic interactions among local moments and their magnetic screening by conduction electrons, the so-called Kondo effect[1]. The small energy scales of these interactions leads to highly tunable ground states, which is ideal for studying strange-metal behaviour. In a variety of systems, tuning this competition leads to a continuous suppression of antiferromagnetic order at a QCP[4]. However, the outcome when a ferromagnetic (FM) transition is suppressed by a non-thermal tuning parameter is generally different[7]. FM QCPs are usually avoided, owing to the occurrence of a first-order transition[11], the intersection of antiferromagnetic phases[12,13], or a Kondo cluster glass phase[14]. This raises the question of whether antiferromagnetic correlations are crucial for realizing strange-metal behaviour.

Early theoretical studies of itinerant ferromagnets[6,8] in the framework of Hertz–Millis–Moriya theory[15] predicted that quantum phase transitions in these materials inevitably become first-order as a consequence

[1]Center for Correlated Matter and Department of Physics, Zhejiang University, Hangzhou, China. [2]Department of Physics and Astronomy, Rutgers University, Piscataway, NJ, USA. [3]Max Planck Institute for Chemical Physics of Solids, Dresden, Germany. [4]Hubbard Theory Consortium, Department of Physics, Royal Holloway, University of London, Egham, UK. [5]Collaborative Innovation Center of Advanced Microstructures, Nanjing University, Nanjing, China. [6]Present address: Center for Quantum Materials and Superconductivity, Department of Physics, Sungkyunkwan University, Suwon, South Korea. [7]These authors contributed equally: Bin Shen, Yongjun Zhang. ✉e-mail: msmidman@zju.edu.cn; coleman@physics.rutgers.edu; hqyuan@zju.edu.cn

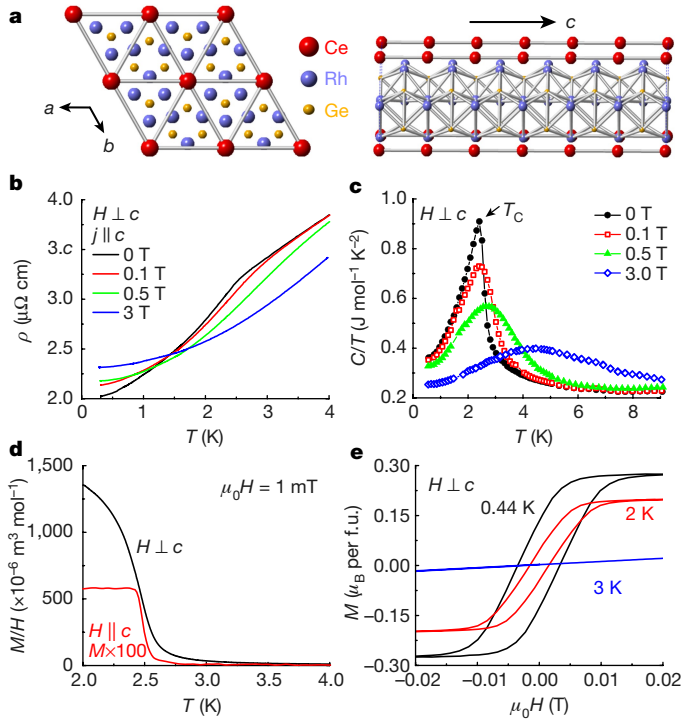

Fig. 1 | Crystal structure and physical properties of $CeRh_6Ge_4$ at ambient pressure. a, Crystal structure of $CeRh_6Ge_4$. The red, blue and yellow atoms denote Ce, Rh, and Ge, respectively. Left, the structure perpendicular to the *a*–*b* plane, where the Ce atoms have a hexagonal arrangement. Right, the structure perpendicular to the chain direction (*c* axis). **b**, **c**, The resistivity $\rho(T)$ (with the current *j* parallel to the *c* axis; **b**) and specific heat as C/T (**c**) versus T for $CeRh_6Ge_4$, in zero field and various fields applied in the *a*–*b* plane. **d**, Temperature dependence of the magnetization of $CeRh_6Ge_4$, as M/H, in a field of 1 mT applied both along the *c* axis and in the *a*–*b* plane, where the data for the *c* axis field are scaled by a factor of 100. **e**, Low-field magnetization loops for fields within the *a*–*b* plane at three temperatures. Below T_C, these exhibit hysteresis loops typical of FM order, whereas at 3 K no hysteresis is observed. f.u., formula unit.

of interactions between the critically scattered electron fields, thereby interrupting the development of quantum criticality. However, the recent discovery of an FM QCP in the heavy-fermion system $YbNi_4P_2$ when tuned by chemical pressure[16] raised the possibility that the FM QCP in these systems is governed by a different universality class involving a breakdown of Kondo screening[17–19]. The negative pressure required to reach the FM QCP of $YbNi_4P_2$ necessarily involves chemical doping of the stoichiometric compound, which introduces disorder, complicating the theoretical interpretation. Disorder suppresses first-order transitions[6], as in the case of $ZrZn_2$, in which early experiments suggested the presence of an FM QCP[20], but improved sample quality led to a first-order transition[21]. Therefore, although the experimental data on $YbNi_4P_2$ suggest the existence of FM QCPs, definitive proof of such behaviour in a quantum ferromagnet requires using hydrostatic instead of chemical pressure. Cerium-based heavy-fermion ferromagnets, in which pressure can cleanly tune the system to a QCP, are ideally suited for such studies.

$CeRh_6Ge_4$ is a heavy-fermion ferromagnet with a Curie temperature[10] $T_C = 2.5$ K. The crystal structure (Fig. 1a) consists of triangular lattices of cerium stacked along the *c* axis[9]. The Ce–Ce separation is much smaller along the *c* axis (3.86 Å) than in the triangular planes (7.15 Å), suggesting a quasi-one-dimensional nature to the magnetism. Under hydrostatic pressure, we find that the FM transition of $CeRh_6Ge_4$ is smoothly suppressed to zero temperature, reaching a QCP at $p_c = 0.8$ GPa.

The temperature dependence of the resistivity $\rho(T)$ and the specific heat (as $C(T)/T$) of single-crystalline $CeRh_6Ge_4$ both show transition anomalies at around $T_C \approx 2.5$ K (Fig. 1b, c). When magnetic fields are applied within the *a*–*b* plane, the transition becomes a broadened crossover, consistent with FM ordering. The low-temperature magnetization divided by the applied field, M/H, is shown in Fig. 1d. Measurements up to 300 K demonstrate that the magnetic easy direction lies within the *a*–*b* plane (Extended Data Fig. 1). On cooling, just above T_C the in-plane M/H undergoes a marked enhancement, typical of FM order. For fields along the *c* axis, M/H abruptly increases at the transition. Magnetization loops below T_C for in-plane fields show hysteresis that is characteristic of FM materials (Fig. 1e). $M(H)$ increases rapidly at low fields, reaching $0.28\mu_B$ per Ce atom for $\mu_0 H = 0.017$ T at 0.44 K (μ_B, Bohr magneton; μ_0, magnetic constant). Upon further increasing the field, there is no hysteresis between up and down field sweeps, and $M(H)$ changes slowly, indicating that $0.28\mu_B$ per Ce atom corresponds to the ordered moment (Extended Data Fig. 1).

The zero-field resistivity and specific-heat coefficient at various pressures are displayed in Fig. 2a, b (see also Extended Data Figs. 3, 4). The evolution of the properties with pressure (p) and the resulting T–p phase diagram are presented in Fig. 3a, b. At T_C the resistivity changes from a linear T-dependent behaviour at high temperature to a T^2-dependent behaviour at low temperatures (Extended Data Fig. 3), where $C(T)/T$ becomes temperature independent. The FM transition, which is suppressed almost linearly by pressure, cannot be detected beyond $p_c = 0.8$ GPa. In the paramagnetic phase above p_c, the aforementioned low-T properties of a Fermi liquid are again observed (Extended Data Figs. 3, 4). The temperature at which this Fermi-liquid behaviour onsets (T_{FL}) increases almost linearly with pressure (Fig. 3b). Both the value of the low-temperature $C(T)/T$ and the A coefficient of the resistivity in $\rho(T) = \rho_0 + AT^2$ (ρ_0, residual resistivity) show an incipient divergence when approaching p_c from the FM or paramagnetic side (Fig. 3a). On both Fermi-liquid sides of the phase diagram, the Kadowaki–Woods ratio A/γ^2 (γ, Sommerfeld coefficient) is 1.49×10^{-6} at ambient pressure and 1.33×10^{-6} μΩ cm mol^2 K^2 mJ^{-2} at 1.12 GPa, which are close to the value for a 4*f*-electron ground-state degeneracy $N = 4$.

At $p_c = 0.8$ GPa, the resistivity is strictly linear in temperature over two orders of magnitude down to at least 40 mK, whereas $C(T)/T \propto \log(T^*/T)$ over nearly an order of magnitude with $T^* = 2.3$ K (T^* is a characteristic temperature of the spin fluctuation energies)[4]; see Fig. 2c. At 60 mK, $C(T)/T$ reaches a very large value of 1.1 J mol^{-1} K^{-2}. Between the FM and paramagnetic phases, there is a fan-shaped strange-metal region with properties similar to canonical antiferromagnetic quantum critical systems such as $CeCu_{6-x}Au_x$[22] and $YbRh_2Si_2$[23]. The pressure dependencies of A and γ (Fig. 3a) follow the residual resistivity ρ_0, which also develops a maximum at p_c, reflecting the presence of quantum critical fluctuations (Extended Data Fig. 3).

At first glance, the strange-metal properties of $CeRh_6Ge_4$ might be attributed to itinerant quantum criticality, because, aside from the absence of a first-order phase transition, Hertz–Millis–Moriya theory predicts a logarithmic Sommerfeld coefficient and a T-linear electron scattering rate, naively equivalent to a T-linear resistivity[4]. However, the scattering off long-wavelength FM fluctuations does not relax electron currents, and once this effect is included, $\rho(T)$ is expected to follow a $T^{5/3}$ dependence at low temperature[4,11]. A T-linear resistivity suggests large-angle scattering, a feature typical of local fluctuations involving a wide range of momenta. Moreover, the strength of the logarithmic divergence in the specific-heat coefficient, from fitting C/T with $(S_0/T^*)\log(T^*/T)$, shows that a large fraction of the local moment entropy, $S_0 \approx (1/10)R\log 2$ (where R is the gas constant), is released over a temperature scale T^* (ref. 4). By contrast, the itinerant Hertz–Millis–Moriya theory predicts $S_0 \propto (q_0/q_F)^3$ where q_0 is the momentum cutoff of the itinerant magnetic fluctuations and q_F is the Fermi momentum (Supplementary Information). Applying this theory to the data then requires $q_0 \approx q_F$, which, by Fourier's theorem, implies that the critical spin fluctuations are local. Together with the absence of a first-order phase transition, these features provide strong evidence in favour of a local QCP.

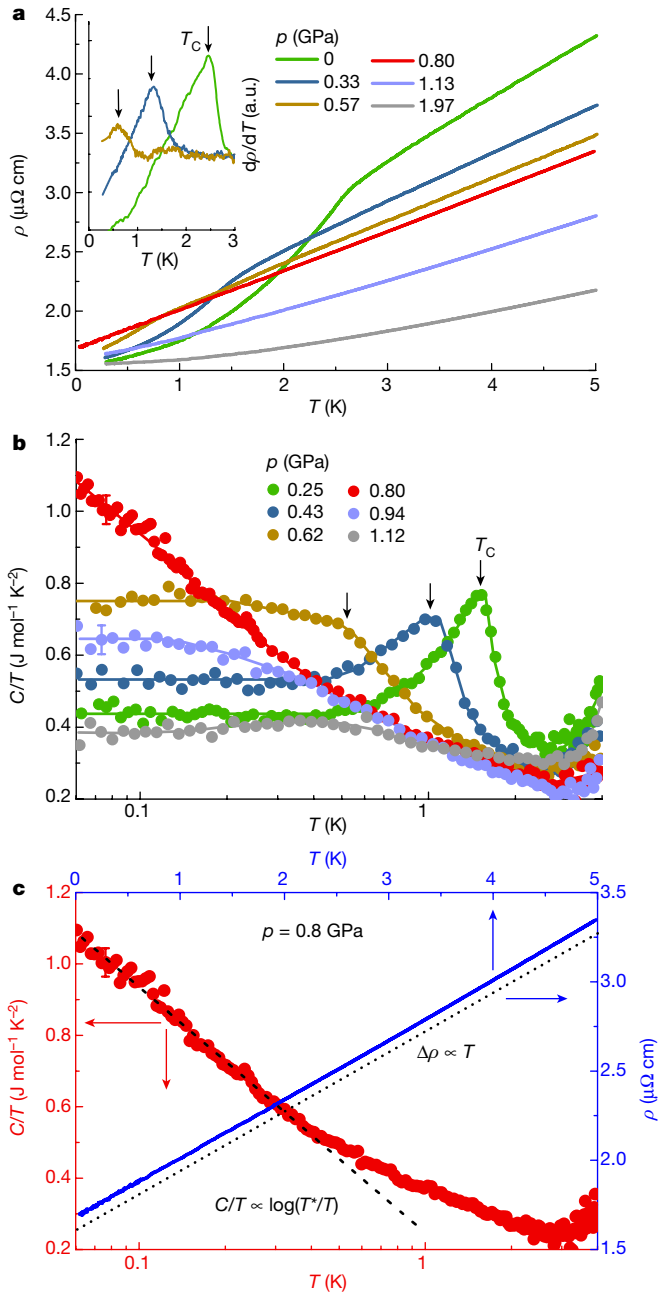

Fig. 2 | Pressure evolution of ferromagnetism in $CeRh_6Ge_4$ and strange-metal behaviour at the QCP. a, Resistivity of $CeRh_6Ge_4$ under various hydrostatic pressures. The FM transition is suppressed by pressure, and is no longer observed at $p_c = 0.8$ GPa (red line). Inset, derivative of $\rho(T)$ at lower pressures; the peak position corresponds to T_C. **b**, Specific heat of $CeRh_6Ge_4$ under hydrostatic pressures. The bulk FM transition is suppressed with pressure, as indicated by the vertical arrows showing the position of T_C. For clarity, not all the data points are displayed. The error bars shown are representative of the scattering of the data at low temperature. A transition to Fermi-liquid behaviour at low temperatures can be observed on either side of p_c, where $C(T)/T$ flattens. **c**, $\rho(T)$ and $C(T)/T$ at $p_c = 0.8$ GPa. $\rho(T)$ exhibits linear behaviour extending from 5 K down to at least 40 mK (dotted line), whereas $C(T)/T$ continues to increase with decreasing temperature, exhibiting a dependence proportional to $\log(T^*/T)$.

In antiferromagnetic heavy-electron metals, the development of T-linear resistivity at the lowest temperatures coincides with an abrupt jump in the Fermi surface volume, accompanied by singular charge fluctuations[24–26]. It has been argued that such a jump in the Fermi surface is caused by an abrupt transformation in the pattern of spin entanglement[5], as the Kondo singlets transform into resonating valence bonds (RVBs) in the spin fluid. This poses a problem, because the spins in a simple ferromagnet are not entangled, which would imply a continuous evolution of the Fermi surface[27]. As shown below, a clue to unravelling this puzzle comes from the unusual aspect that $CeRh_6Ge_4$ develops a strange-metal phase at an FM QCP, similar to that observed for the non-stoichiometric material $YbNi_4P_{2-x}As_x$[16].

Apart from their quasi-one-dimensional nature, a common feature of these two materials is an easy-plane anisotropy. In such systems, the magnetic-order parameter is no longer conserved and will develop marked zero-point fluctuations, which are probably responsible for the severely reduced magnetic moment. This can be seen clearly in a two-site example where the magnetization is perpendicular to the quantization (z) axis of the spins. The ordered phase is a product state that can be expanded in terms of triplets,

$$\frac{|\uparrow_i\rangle + |\downarrow_i\rangle}{\sqrt{2}}\frac{|\uparrow_j\rangle + |\downarrow_j\rangle}{\sqrt{2}} = \frac{|\uparrow_i\uparrow_j\rangle + |\downarrow_i\downarrow_j\rangle}{2} + \frac{1}{\sqrt{2}}\frac{|\uparrow_i\downarrow_j\rangle + |\downarrow_i\uparrow_j\rangle}{\sqrt{2}} \quad (1)$$

where i and j are site indices. An easy-plane anisotropy projects out the equal-spin pairs on the right-hand side, creating a triplet valence bond. In a lattice, the same effect creates a quantum superposition of triplet pairs, forming a triplet RVB state, $|\mathrm{tRVB}\rangle$. Hence, easy-plane anisotropy in FM systems has the same role as magnetic frustration in antiferromagnetic systems, injecting a macroscopic entanglement into the ground state. This leads us to hypothesize that the strange-metal behaviour at the FM QCP has its origins in the magnetic anisotropy.

To test these ideas, we have studied a simplified Kondo lattice model with nearest-neighbour FM couplings with easy-plane anisotropy of the form $-J^{ij}_{xy}(S^x_iS^x_j + S^y_iS^y_j) - J^{ij}_zS^z_iS^z_j$ on a tetragonal lattice, consisting of spin chains along the c direction with weak inter-chain couplings (see Supplementary Information). Here, $S^{x,y,z}_j$ are the x, y and z components of the spin at site j, and J^{ij}_{xy} and J^{ij}_z are the magnetic couplings between the spins at sites i and j. When the chains are weakly coupled, our simulations indicate the development of a second-order phase transition, whereas at higher couplings a first-order phase transition develops. This feature is in agreement with the current observations of FM QCPs developing in quasi-one-dimensional systems. We assume $J_{xy} > J_z$, which has a dual effect: it converts the model into an easy-plane x–y ferromagnet, and generates triplet RVBs. Also, the anisotropy changes the magnetic dispersion at low momenta from quadratic to linear (see Supplementary Information). By switching on the Kondo screening[26–28] we can then tune the model to the QCP.

Our calculations take advantage of a Schwinger-boson representation of the magnetic moments, which enables us to examine both the magnetic and Kondo-screened parts of the phase diagram, and the QCP that links them together (Fig. 3c). The key feature of this approach is a representation of the spins as bosonic spinons, enabling a dynamical description of the Kondo effect in which neutral local moments fractionalize into negatively charged electrons, leaving behind positively charged Kondo singlets. In the ordered phase, a majority of the moments are aligned, although some form triplet RVB pairs with their neighbours. In an isotropic ferromagnet, the continuous growth of magnetization away from the QCP indicates a continuous change in the fraction of Kondo-screened moments, or a continuous evolution of the Fermi surface. However, when the moments entangled within tRVB states are abruptly released into the Fermi sea, we find (see Supplementary Information) that there is a jump in the Fermi surface volume. The resulting QCP is a plasma in which the Kondo singlets, the electrons and the RVB bonds are in a state of critical dynamical equilibrium, giving rise to singular spin and charge fluctuations as well as a specific-heat coefficient that is logarithmic in temperature (Supplementary Information), in agreement with our experimental results.

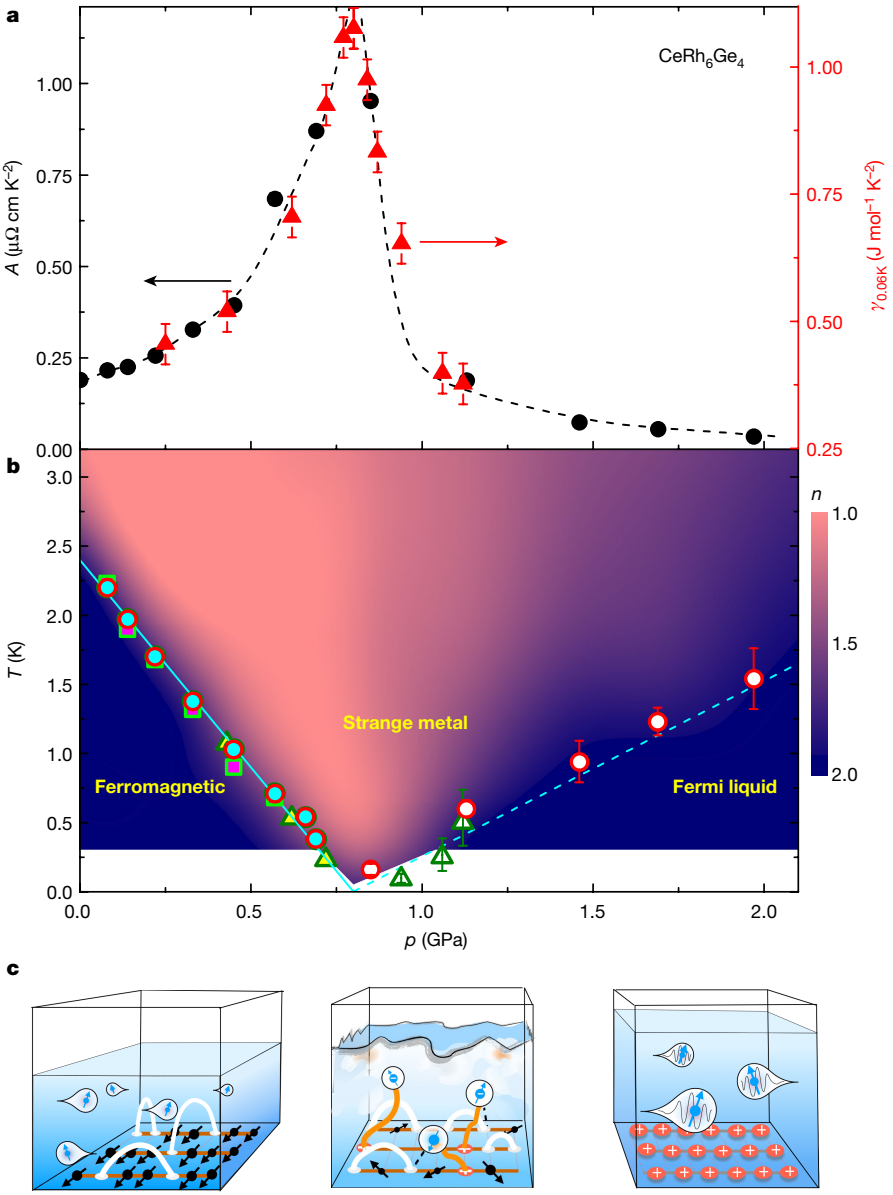

Fig. 3 | Phase diagram of $CeRh_6Ge_4$ under pressure. a, Pressure dependence of the A coefficient of the T^2 term from the resistivity and Sommerfeld coefficient γ (as C/T at 60 mK), which shows a pronounced maximum near the QCP. The error bars for the A coefficient are smaller than the symbols. For γ, the errors correspond to the scattering of the low-T data. The dashed line is a guide to the eye. **b**, T–p phase diagram of $CeRh_6Ge_4$. The circles, triangles and squares for pressures below p_c denote T_C derived from the resistivity, specific heat (d.c. method), and a.c. heat capacity (Extended Data Fig. 5), respectively. The corresponding symbols above p_c mark T_{FL}, below which Fermi-liquid behaviour occurs. The FM transition is suppressed by pressure until the system reaches a QCP at $p_c \approx 0.8$ GPa. Below T_C, and at higher pressures below T_{FL}, Fermi-liquid ground states develop. The colours denote the exponent of $\rho(T)$ calculated as $n = \mathrm{d}(\log(\rho - \rho_0))/\mathrm{d}(\log T)$, where the Fermi-liquid states with $n = 2$ are dark blue, and the strange-metal phase near the QCP with $n = 1$ is shown in pink. **c**, Schematic representation of different phases. In the ordered phase (left), most of the spins are ordered in the plane, although some have RVB bonds. The Fermi surface is small, as represented by the volume of the conduction sea. In the paramagnetic Fermi-liquid phase (right), all the spins are 'ionized' to form heavy electrons that expand the Fermi sea. A background of positively charged singlets are left behind. At the QCP (centre), the system is in a dynamical critical equilibrium in which the moments are fluctuating and the Kondo screening by the conduction electron competes with RVBs for the entanglement. In this region, critical fluctuations strongly scatter the conduction electrons.

Our findings of a pressure-induced QCP in $CeRh_6Ge_4$ demonstrate that an FM system can develop a continuous quantum phase transition in the absence of disorder, a result that at present can only be understood in the framework of local quantum criticality, where Kondo screening is suppressed to zero at the QCP. The observation of strange-metal behaviour at finite temperatures above the QCP—that is, T-linear resistivity and a specific-heat coefficient that is logarithmically divergent in T—expands the scope of this phenomenon to encompass ferromagnets. Central to the strange-metal behaviour in a ferromagnet is a small abrupt jump in the Fermi surface volume. An experimental observation of such a jump would be an unambiguous test of Kondo breakdown, because there is no unit-cell doubling at an FM phase transition.

Finally, spin-triplet superconducting pairing states have been proposed in FM heavy-fermion systems such as UGe_2[29] and URhGe[30]. Although there is no sign of superconductivity in $CeRh_6Ge_4$ down to 40 mK, it is probable that at sufficiently low temperatures the triplet RVB states that are already present in the critical regime will migrate into the conduction band as a triplet superconducting condensate.

Online content

Any methods, additional references, Nature Research reporting summaries, source data, extended data, supplementary information, acknowledgements, peer review information; details of author contributions and competing interests; and statements of data and code availability are available at https://doi.org/10.1038/s41586-020-2052-z.

1. Gegenwart, P., Si, Q. & Steglich, F. Quantum criticality in heavy-fermion metals. *Nat. Phys.* **4**, 186–197 (2008).
2. Daou, R. et al. Linear temperature dependence of resistivity and change in the Fermi surface at the pseudogap critical point of a high-T_c superconductor. *Nat. Phys.* **5**, 31–34 (2008).
3. Legros, A. et al. Universal *T*-linear resistivity and Planckian dissipation in overdoped cuprates. *Nat. Phys.* **15**, 142–147 (2019).
4. Stewart, G. R. Non-Fermi-liquid behavior in *d*- and *f*-electron metals. *Rev. Mod. Phys.* **73**, 797–855 (2001).
5. Senthil, T., Vojta, M. & Sachdev, S. Weak magnetism and non-Fermi liquids near heavy-fermion critical points. *Phys. Rev. B* **69**, 035111 (2004).
6. Belitz, D., Kirkpatrick, T. R. & Vojta, T. First-order transitions and multicritical points in weak itinerant ferromagnets. *Phys. Rev. Lett.* **82**, 4707–4710 (1999).
7. Brando, M., Belitz, D., Grosche, F. M. & Kirkpatrick, T. R. Metallic quantum ferromagnets. *Rev. Mod. Phys.* **88**, 025006 (2016).
8. Chubukov, A. V., Pépin, C. & Rech, J. Instability of the quantum critical point of itinerant ferromagnets. *Phys. Rev. Lett.* **92**, 147003 (2004).
9. Vosswinkel, D., Niehaus, O., Rodewald, U. C. & Pöttgen, R. Bismuth flux growth of $CeRh_6Ge_4$ and $CeRh_2Ge_2$ single crystals. *Z. Naturforsch. B* **67**, 1241–1247 (2012).
10. Matsuoka, E. et al. Ferromagnetic transition at 2.5 K in the hexagonal Kondo-lattice compound $CeRh_6Ge_4$. *J. Phys. Soc. Jpn* **84**, 073704 (2015).
11. Pfleiderer, C., McMullan, G. J., Julian, S. R. & Lonzarich, G. G. Magnetic quantum phase transition in MnSi under hydrostatic pressure. *Phys. Rev. B* **55**, 8330–8338 (1997).
12. Süllow, S., Aronson, M. C., Rainford, B. D. & Haen, P. Doniach phase diagram, revisited: from ferromagnet to Fermi liquid in pressurized $CeRu_2Ge_2$. *Phys. Rev. Lett.* **82**, 2963–2966 (1999).
13. Brando, M. et al. Logarithmic Fermi-liquid breakdown in $NbFe_2$. *Phys. Rev. Lett.* **101**, 026401 (2008).
14. Westerkamp, T. et al. Kondo-cluster-glass state near a ferromagnetic quantum phase transition. *Phys. Rev. Lett.* **102**, 206404 (2009).
15. Sachdev, S. *Quantum Phase Transitions* 2nd edn (Cambridge Univ. Press, 2011).
16. Steppke, A. et al. Ferromagnetic quantum critical point in the heavy-fermion metal $YbNi_4(P_{1-x}As_x)_2$. *Science* **339**, 933–936 (2013).
17. Custers, J. et al. The break-up of heavy electrons at a quantum critical point. *Nature* **424**, 524–527 (2003).
18. Schröder, A. et al. Onset of antiferromagnetism in heavy-fermion metals. *Nature* **407**, 351–355 (2000).
19. Yamamoto, S. J. & Si, Q. Metallic ferromagnetism in the Kondo lattice. *Proc. Natl Acad. Sci. USA* **107**, 15704–15707 (2010).
20. Smith, T. F., Mydosh, J. A. & Wohlfarth, E. P. Destruction of ferromagnetism in $ZrZn_2$ at high pressure. *Phys. Rev. Lett.* **27**, 1732–1735 (1971).
21. Uhlarz, M., Pfleiderer, C. & Hayden, S. M. Quantum phase transitions in the itinerant ferromagnet $ZrZn_2$. *Phys. Rev. Lett.* **93**, 256404 (2004).
22. Löhneysen, H. v. et al. Non-Fermi-liquid behavior in a heavy-fermion alloy at a magnetic instability. *Phys. Rev. Lett.* **72**, 3262–3265 (1994).
23. Trovarelli, O. et al. $YbRh_2Si_2$: pronounced non-Fermi-liquid effects above a low-lying magnetic phase transition. *Phys. Rev. Lett.* **85**, 626–629 (2000).
24. Paschen, S. et al. Hall-effect evolution across a heavy-fermion quantum critical point. *Nature* **432**, 881–885 (2004).
25. Shishido, H., Settai, R., Harima, H. & Ōnuki, Y. A drastic change of the Fermi surface at a critical pressure in $CeRhIn_5$: dHvA study under pressure. *J. Phys. Soc. Jpn* **74**, 1103–1106 (2005).
26. Komijani, Y. & Coleman, P. Emergent critical charge fluctuations at the Kondo breakdown of heavy fermions. *Phys. Rev. Lett.* **122**, 217001 (2019).
27. Komijani, Y. & Coleman, P. Model for a ferromagnetic quantum critical point in a 1D Kondo lattice. *Phys. Rev. Lett.* **120**, 157206 (2018).
28. Wang, J., Chang, Y.-Y., Mou, C.-Y., Kirchner, S. & Chung, C.-H. Quantum phase transition in a two-dimensional Kondo–Heisenberg model: a Schwinger-boson large-*N* approach. Preprint at http://arxiv.org/abs/1901.10411 (2019).
29. Saxena, S. S. et al. Superconductivity on the border of itinerant-electron ferromagnetism in UGe_2. *Nature* **406**, 587–592 (2000).
30. Lévy, F., Sheikin, I., Grenier, B. & Huxley, A. D. Magnetic field-induced superconductivity in the ferromagnet URhGe. *Science* **309**, 1343–1346 (2005).

Publisher's note Springer Nature remains neutral with regard to jurisdictional claims in published maps and institutional affiliations.

© The Author(s), under exclusive licence to Springer Nature Limited 2020

Methods

Crystal growth and characterization

Needle-shaped single crystals of $CeRh_6Ge_4$ were grown using a bismuth flux[9]. The elements were combined in a molar ratio of Ce:Rh:Ge:Bi of 1:6:4:150, and sealed in an evacuated quartz tube. The tube was heated and held at 1,100 °C for 10 h, then cooled at 3 °C per hour to 500 °C. The tube was then removed, and centrifuged to remove the excess bismuth. The orientation of the crystals was determined using single-crystal X-ray diffraction, and the chemical composition was confirmed using energy-dispersive X-ray spectroscopy. The samples measured under pressure had typical values of $\rho_0 \approx 1.6\ \mu\Omega$ cm and a residual-resistance ratio of RRR = $\rho(300\ \mathrm{K})/\rho(0.3\ \mathrm{K}) \approx 45$ (Extended Data Fig. 2).

Physical property measurements

Magnetization measurements were performed using a Magnetic Property Measurement System (Quantum Design). The heat capacity at ambient pressure was measured down to 0.4 K in applied magnetic fields up to 14 T, using a Quantum Design Physical Property Measurement System (PPMS) with a ^{3}He insert, using the standard relaxation method. Specific-heat experiments under pressure were carried out using a copper beryllium piston-cylinder-type pressure cell[31]. The sample and a piece of lead as pressure gauge were put in a teflon capsule together with Flourinert serving as a liquid pressure-transmitting medium. The capsule was then mounted inside the pressure cell. The heat capacity of the whole assembly was determined by a compensated heat-pulse method in a dilution refrigerator (Oxford Instruments) down to temperatures of 60 mK. To obtain the heat capacity of the sample the addenda has been recorded in a separate measurement run and subtracted for each pressure from the data obtained of the whole setup including the sample. The pressure inside the cell was determined by the pressure-induced shift of the superconducting transition temperature of the piece of lead, which was measured in a Magnetic Property Measurement System (Quantum Design). The magnetic field was removed in an oscillating fashion to reduce the remanent field (<3 Oe) of the superconducting magnet. The remaining effect on the superconducting transition temperature was compensated for by determining the shift of the superconducting transition of the lead inside the pressure cell with respect to a reference piece fixed to the outside. Electrical transport and a.c. calorimetry measurements under pressure were carried out in a piston-cylinder clamp-type cell with Daphne oil 7373 as a pressure-transmitting medium. The pressure was also determined from the superconducting transition of lead. The resistivity was measured using the four-contact configuration between 0.04 K and 300 K. The measurements were performed down to 1.9 K, 0.4 K and 0.04 K in a PPMS, ^{3}He refrigerator and dilution refrigerator, respectively. Data obtained from these measurements are all consistent.

Data availability

All the data supporting the findings are available from the corresponding authors upon reasonable request.

31. Nicklas, M. in *Strongly Correlated Systems: Experimental Techniques* (eds Mancini, F. & Avella, A.) 180, 173–204 (Springer, 2015).

Acknowledgements We thank C. Krellner and M. Brando for discussions, G. Cao and Z. Wang for assisting with ^{3}He-SQUID measurements and X. Xiao for assistance with single-crystal X-ray diffraction. This work was supported by the National Key R&D Program of China (grants 2017YFA0303100, 2016YFA0300202), the National Natural Science Foundation of China (grants U1632275, 11974306), the Science Challenge Project of China (grant number TZ2016004) and the National Science Foundation of the United States of America, grant number DMR-1830707.

Author contributions H.Y. conceived the study and led the project. The crystals were grown by Y.Z. and H.L. Measurements of the properties at ambient pressure, as well as measurements of the electrical resistivity and a.c. specific heat under pressure, were performed by B.S., Y.Z., A.W., Y.C., Z.N., R.L., X.L. and H.Y. The quasi-adiabatic specific-heat measurements under hydrostatic pressure were measured by R.B. and M.N. The experimental data were analysed by B.S., Y.Z., M.N., H.L., M.S., F.S. and H.Y. Theoretical calculations were performed by Y.K. and P.C. The manuscript was written by Y.K., M.S., F.S., P.C. and H.Y. All authors participated in discussions.

Competing interests The authors declare no competing interests.

Additional information
Supplementary information is available for this paper at https://doi.org/10.1038/s41586-020-2052-z.
Correspondence and requests for materials should be addressed to M.S., P.C. or H.Y.
Reprints and permissions information is available at http://www.nature.com/reprints.

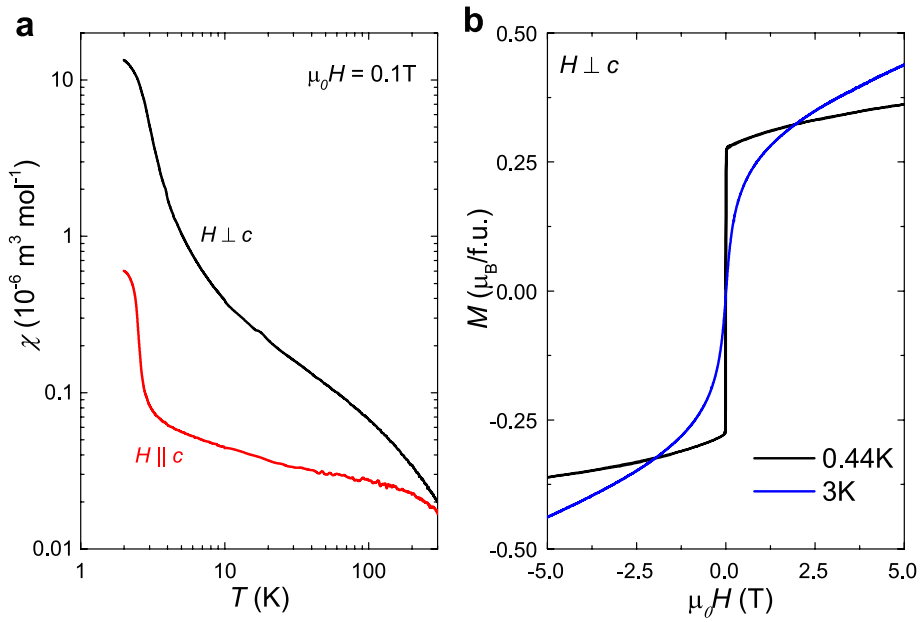

Extended Data Fig. 1 | Magnetic susceptibility and field-dependent magnetization. a, Temperature dependence of the magnetic susceptibility ($\chi(T)$) of $CeRh_6Ge_4$ in a field of 0.1 T applied both along the *c* axis and in the *a*–*b* plane, where both axes are plotted on a logarithmic scale. $\chi(T)$ is anisotropic across the whole temperature range; the *a*–*b* plane corresponds to the easy direction. **b**, Magnetization loops measured at 3 K and 0.44 K, above and below T_C, respectively. In the FM state, the magnetization increases rapidly at low fields, reaching a value of around 0.28μ_B per Ce atom, which probably corresponds to the ordered moment, whereas at higher fields the magnetization increases more slowly.

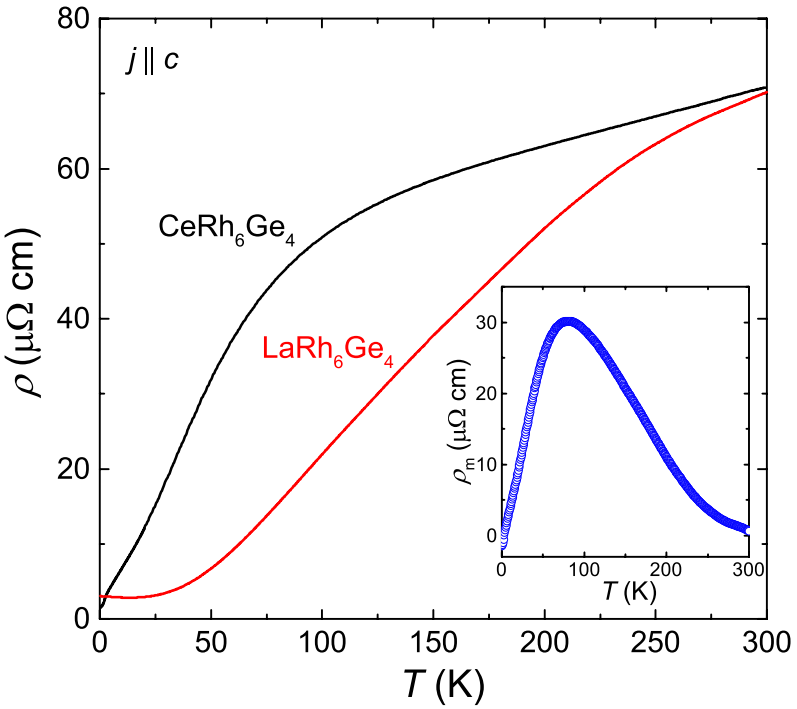

Extended Data Fig. 2 | Temperature-dependent resistivity at ambient pressure. Temperature dependence of the resistivity ($\rho(T)$) of $CeRh_6Ge_4$ and for the non-magnetic analogue $LaRh_6Ge_4$, with the current along the *c* axis. The inset shows the magnetic contribution to the resistivity of $CeRh_6Ge_4$ (ρ_m), obtained from subtracting the data of $LaRh_6Ge_4$. This exhibits a broad maximum at around 80 K, probably as a consequence of both the crystalline electric field and Kondo effects.

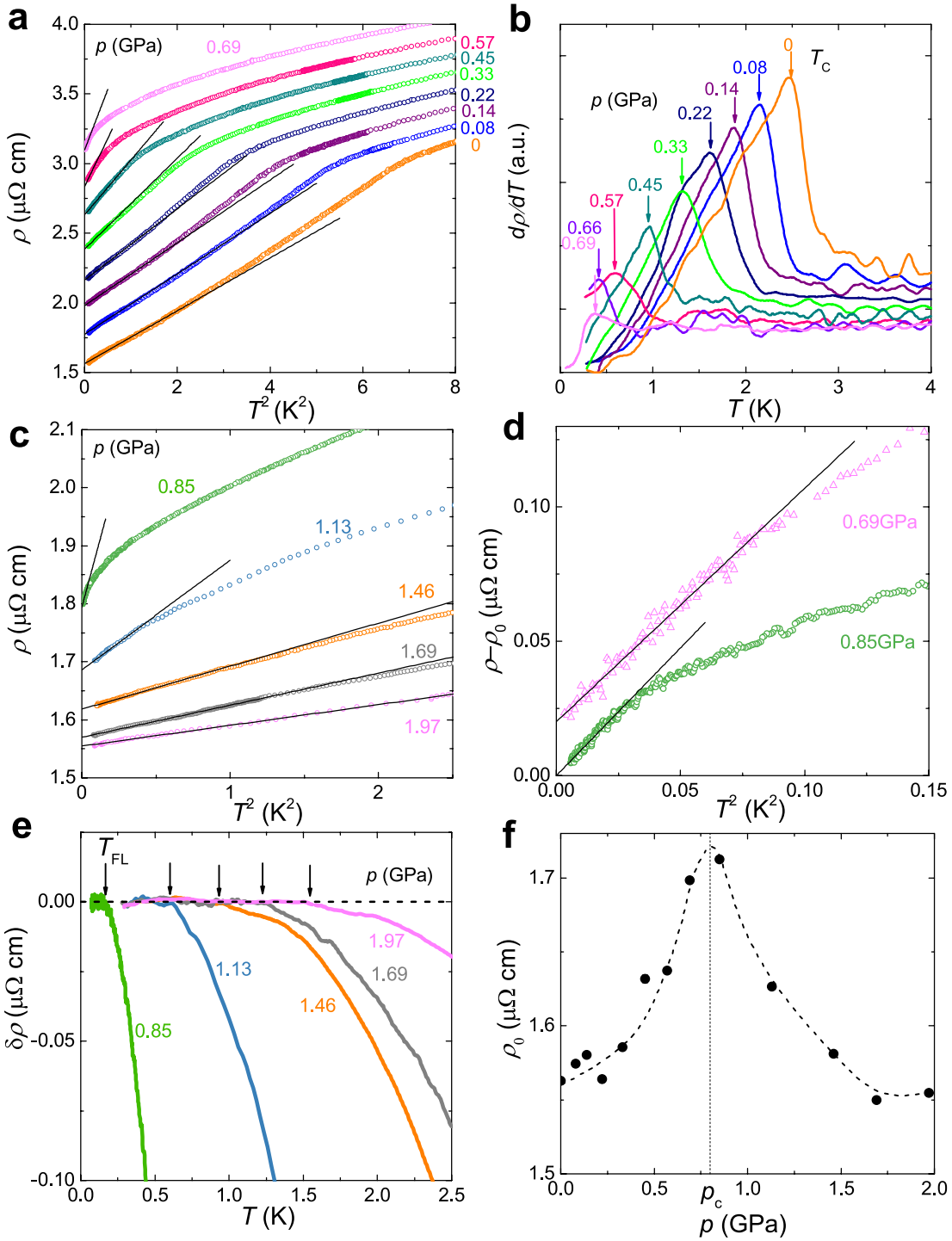

Extended Data Fig. 3 | Analysis of the resistivity under pressure. a, Low-temperature $\rho(T)$ of $CeRh_6Ge_4$ versus T^2 under pressures up to 0.69 GPa. For clarity, the data at consecutive pressures are offset vertically by 0.2 μΩ cm. The low-temperature data in the magnetic state was fitted with a quadratic temperature dependence, $\rho(T) = \rho_0 + AT^2$, as shown by the solid black lines. **b**, The corresponding derivative $d\rho(T)/dT$, where the position of T_C was determined at each pressure from the position of the maximum, as indicated by the vertical arrows. a.u., arbitrary units. **c**, Low-temperature $\rho(T)$ versus T^2 of $CeRh_6Ge_4$ at pressures above the QCP; the data at consecutive pressures are offset vertically by 0.02 μΩ cm. The solid lines show the quadratic temperature dependence, indicating the occurrence of Fermi-liquid behaviour at low temperatures. **d**, Low-temperature enlargement of $\rho(T) - \rho_0$ for two pressures either side of the QCP, where the data at 0.69 GPa are vertically offset by 0.02 μΩ cm. **e**, Resistivity as a function of temperature plotted as $\delta\rho = \rho - \rho_{FL}$, for various pressures p. ρ_{FL} is the Fermi-liquid contribution to the resistivity, obtained from fitting the low-temperature $\rho(T)$ with a quadratic temperature dependence. The deviation of $\delta\rho$ from zero indicates the onset of non-Fermi-liquid behaviour, and hence corresponds to T_{FL}, as marked by the vertical arrows. **f**, Pressure dependence of the residual resistivity ρ_0, obtained from analysing the low-temperature $\rho(T)$ at various pressures, and where the error bars are smaller than the symbol size. This quantity reaches a maximum around the QCP.

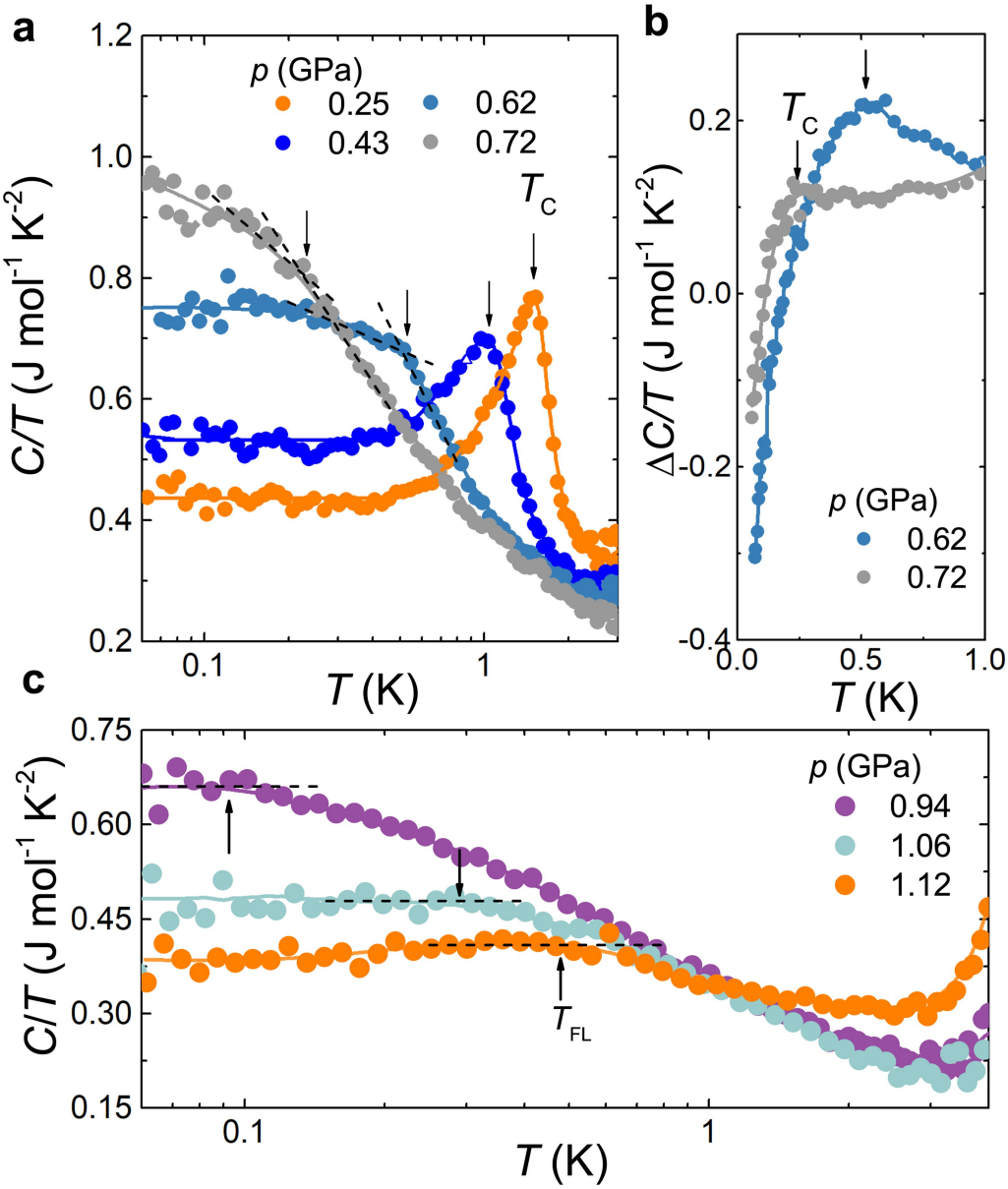

Extended Data Fig. 4 | Analysis of the heat capacity under pressure. **a**, Temperature dependence of the absolute value of the heat capacity as C/T, at various pressures below p_c. For pressures up to 0.72 GPa, T_C can be detected, as marked by the vertical arrows. At lower pressures this is determined from the peak positions, whereas close to p_c it is determined by the intersection of the solid lines indicated in the figure. **b**, The data for two pressures near p_c, after subtracting the data taken at 0.8 GPa to remove the logarithmic contribution to C/T. In both cases, the peak position of $\Delta C/T$ is in good agreement with the value of T_C obtained from **a**. **c**, Low-temperature $C(T)/T$ for three pressures above the QCP. The strong increase with decreasing temperature corresponds to non-Fermi-liquid behaviour, whereas the flattening of $C(T)/T$ at low temperatures corresponds to the onset of Fermi-liquid behaviour. The position of the temperature below which Fermi-liquid behaviour occurs, T_{FL}, is highlighted by the vertical arrows, and is determined from the deviation from the near-temperature-independent behaviour marked by the dashed lines.

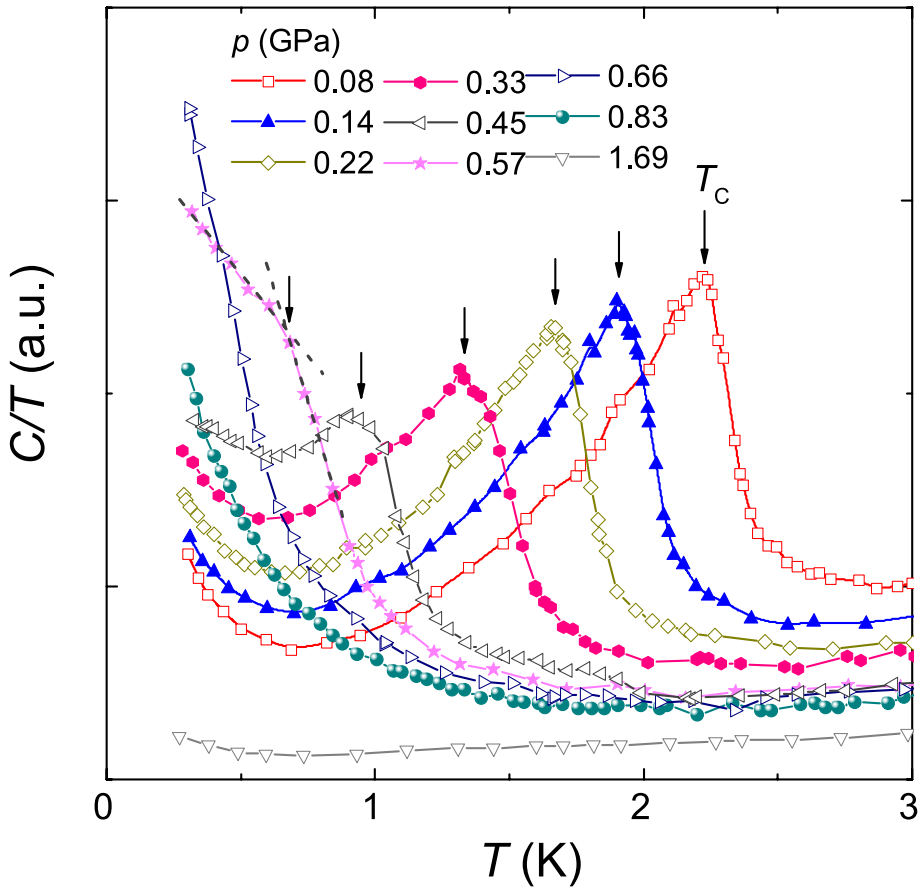

Extended Data Fig. 5 | The a.c. heat capacity under pressure. The a.c. heat capacity as C/T at various pressures up to 1.69 GPa. For pressures below 0.83 GPa, the position of T_C is marked by the vertical arrows. The dashed lines show the construction used to determine T_C near p_c. At 0.83 GPa, no transition is detected down to the lowest measured temperature, 0.3 K; instead, C/T continues to increase with decreasing temperature. At 1.69 GPa, well above the QCP, C/T shows little temperature dependence. a.u., arbitrary units.